sciendo **Transactions on Aerospace Research** eISSN 2545-2835, VOL. 267, NO. 2/2022, 31-61
DOI: 10.2478/tar-2022-0009

DEVELOPMENT OF A FLIGHT SIMULATOR FOR CONCEPTUAL AIRCRAFT DESIGN AND SIZING

Kai San Hon [1*], **Stanislav Karpuk** [2], **Daqing Yang** [1], **Ali Elham** [2]
[1] Department of Aeronautics, Faculty of Engineering, Imperial College London, London SW7 2AZ, United Kingdom
[2] Institute of Aircraft Design and Lightweight Structures, Faculty of Mechanical Engineering, Technische Universität Braunschweig, 38106 Braunschweig, Germany

Abstract

This article describes the development of a flight simulator module within the ADEMAO aircraft design framework to investigate the effects of novel airframe and propulsion technologies on new generations of aircraft. Methods used to develop and integrate the fight simulator into the overall design framework are described. The simulator is validated based on existing data from the Convair CV-880M and is then used to analyze an example case of a conceptual medium-range aircraft with advanced airframe technologies designed in the Sustainable and Energy-Efficient Aviation research cluster at the Institute of Aircraft Design and Lightweight Structures at the Technische Universität Braunschweig. Results show the deficiencies of the medium-range aircraft in short-period pitch and Dutch roll performance, and recommendations for modifications to the conceptual medium-range aircraft are drafted.

Keywords: flight dynamics, flight smulation, aircraft design
Type of the work: research article

1. INTRODUCTION

Significant climate changes and the potential environmental impact due to increased transportation in the near future have motivated many industries to reduce CO_2 and NO_x emissions. As a major transportation method, the aviation industry also follows the trend towards reducing emissions in new generations of aircraft, while continuous improvements in airframe and engine technologies in commercial aircraft are improving aircraft efficiency. However, the potential increase in the volume of air transportation observed over recent years may still lead to an increase in overall CO_2 and NO_x emissions if travelling trends maintain similar growth rates. Based on Flightpath 2050 [4], challenging recommendations to reduce total aircraft emissions by 2050 have been proposed. However, satisfying such goals does not seem possible using conventional airframes and propulsion systems with similar improvements in their technologies. Alternative environmentally friendly energy sources, novel airframe technologies, and more fuel-efficient aircraft configurations must be considered and investigated to understand what potential energy-efficient aircraft may look like.

The SE2A (Sustainable and Energy-Efficient Aviation) Cluster of Excellence is focused on the development of next-generation airframes and propulsion technologies, as well as assessments of important operational issues such as air traffic control, noise emission, etc. The cluster is divided into three major branches as shown in Figure 1. The second branch (ICA B) specializes in the development

* Corresponding Author: kai.hon17@imperial.ac.uk
ARTICLE HISTORY **Received** 2021-12-09 **Revised** 2022-01-26 **Accepted** 2022-04-01

of new airframe technologies, and the investigation and assessment of aircraft configurations featuring these technologies. Three aircraft with advanced airframe and propulsion technologies are being developed within the research group: a short-range regional propeller aircraft, a mid-range airliner, and a long-range airliner. Due to the time constraints in this research project, however, only the mid-range airliner will be used as an example case. Figure 2 shows a schematic representation of these aircraft.

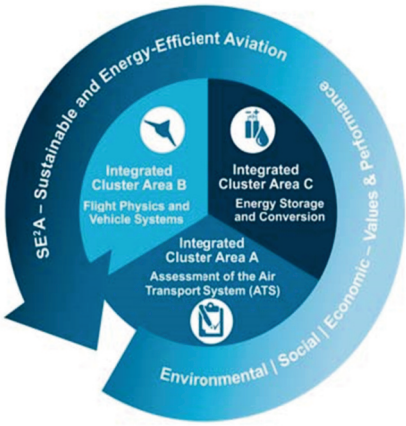

Figure 1. SE2A cluster structure.

Figure 2. A family of energy-efficient aircraft considered within the SE2A cluster.

Analyzing aircraft with various technologies and proposed configurations that may significantly deviate from conventional aircraft, a multi-fidelity approach is required. To perform these tasks, a Multi-layer Aircraft Design Framework ADEMAO is being developed, whose structure is shown in Figure 3. ADEMAO is divided into four major modules that are responsible for specific design tasks. The first module initializes the aircraft configuration and performs the tasks required to size the aircraft. The second module focuses on the generation of surrogate models that will be constructed within the cluster based on technological trends. Finally, the two remaining modules perform higher fidelity analyses and optimization, so complex physical phenomena can be captured well. All the modules are interconnected, so the information can travel among modules and can be used during the design process.

The Design initiator module is built around the aircraft design environment [16] which performs the flight mission simulation. Within the cluster, SUAVE has been extended to perform initial aircraft sizing based on the sizing chart and to perform the necessary trade studies, as well as being coupled with the MATLAB Genetic algorithm to perform multi-disciplinary design optimization.

Since the aircraft designed feature advanced technologies and may not have conventional configurations, careful assessment of flight dynamic characteristics is required at early design stages so sufficient information about the configuration can be obtained to make adequate design decisions. Consequently, a flight simulator with sufficient capabilities is required to initialize the aircraft considered within the cluster.

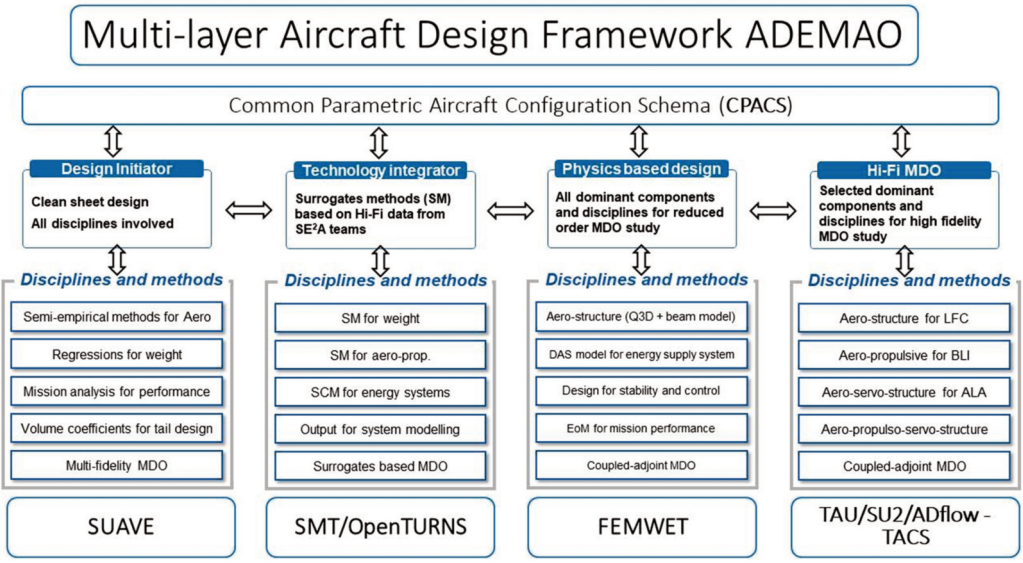

Figure 3. Structure of the aircraft design framework ADEMAO.

2. INTEGRATION OF THE FLIGHT SIMULATOR INTO THE AIRCRAFT INITIALIZATION FRAMEWORK

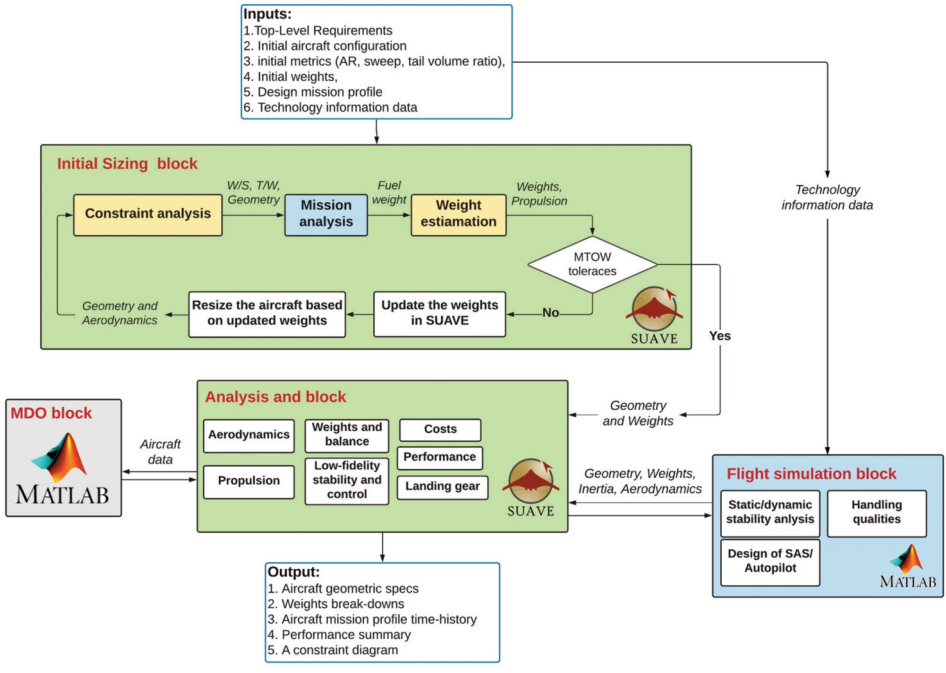

Figure 4. Aircraft initializer structure.

The integration of the flight simulator block into the overall aircraft sizing framework is shown in Figure 4. If the aircraft was not initially sized, the initial aircraft sizing and analysis refinement with a multi-disciplinary design optimization (MDO) option is performed. Then, the geometry, weights, inertia properties, and other analysis components (for example, higher fidelity aerodynamic surrogates) are imported into the flight simulator. If the aircraft has already been sized, all the information available goes directly into the simulator. In addition, since aircraft investigated under the SE2A cluster feature advanced airframe technologies, the flight simulator is capable of accepting data related to these technologies. Data can be imported either in the form of surrogate models or a set of constant coefficient gains depending on the technology's maturity within the cluster. Based on the outcomes of the flight simulations, stability and control analyses, and investigation of handling qualities, the information obtained is used to update the aircraft configuration using SUAVE or is passed directly to the output for the final post-processing and data export.

3. FLIGHT SIMULATOR DEVELOPMENT

3.1. Flight Dynamics Model

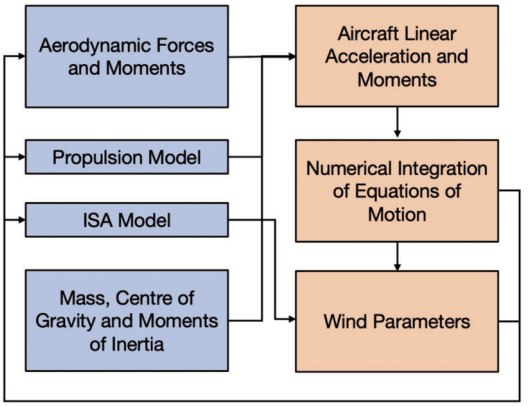

Figure 5. Flight dynamics model of the flight simulator.

To develop the flight simulator, the MATLAB/Simulink environment was used. Figure 5 shows the flight simulator structure, its key modules, and their connections. The aerodynamic forces and moments module takes the wind parameters and calculates the aerodynamic forces and moments exerted on the aircraft. The three aerodynamic forces simulated in the model using a body-axial frame are lift, side force and drag, whereas the three moments simulated are the pitching, rolling and yawing moments. The model also accounts for the forces and moments produced by the control surfaces and the deployment of high-lift devices (HLD), and accepts corrections based either on technology surrogates or constant gains assumed within the excellence cluster.

The propulsion module simulates the thrust exerted on the aircraft by the propulsion system with inputs from the wind parameters, and the modeling method depends on the type of engine used on a given aircraft. Thrust and power lapses from altitude and Mach effects are also considered for accurate modeling. Furthermore, the module features the capability to simulate inoperative engines to test for compliance with regulations, as most regulations require test results such as take-off and landing performance with one-engine-inoperative.

The key parameters provided by the mass module are the mass of the aircraft, the position of the center of gravity, and the moments of inertia. These parameters are required to model the aircraft's linear and angular accelerations. These parameters vary in flight as fuel is consumed and the variations should be accounted for if the flight simulator intends to simulate long flight periods, though the significance reduces if the simulator is only intended for simulating point performance and short flight periods.

An atmospheric module is responsible for all necessary calculations regarding free-stream flight conditions and uses classical standard atmosphere relations.

The parameters provided by the four models above are collected into the calculator for the linear accelerations and moments of the aircraft based on the differential equations of motion, the results of which are collected into the calculator that integrates the equations of motion to calculate the velocity, position and attitude of the aircraft while also taking into altitude effects using results from the ISA model. These results are then fed into the four modules to produce new results from a new iteration.

3.2. Aerodynamic Model Development

Look-up tables for the aerodynamic coefficients CL, CD, CY, Cl, Cm and Cn are used to obtain the aerodynamic forces and moments exerted on the aircraft. By using such tables, the user not only has the option to increase or decrease the fidelity level of the data at different design stages of the aircraft, but also the ability to simulate different aircraft types that will be designed in the institute in the future.

To assist conceptual aircraft design, a MATLAB script has been designed such that it will run an AVL model of the concept aircraft and output look-up tables of the aerodynamic coefficients in the 4-dimensional format (The force and moment coefficients as a function of α, β, Mach and Flap Angle) required by the simulator. The coefficients collected from AVL can be divided into three groups: steady-state, perturbed-state, and contributions from control surfaces, and are categorized as shown in Table 1.

Table 1. Aerodynamic Force and Moment Coefficients collected from AVL for the simulator.

Category	**Coefficients**
Steady-State	C_L, C_D, C_Y, C_l, C_m, C_n, C_{L_α}, C_{Y_β}, C_{l_β}, C_{m_α}, C_{n_β}
Perturbed-State	C_{L_q}, C_{m_q}, C_{l_p}, C_{l_r}, C_{n_p}, C_{n_r}
Controls	$C_{L_{\delta_e}}$, $C_{m_{\delta_e}}$, $C_{l_{\delta_a}}$, $C_{l_{\delta_r}}$, $C_{Y_{\delta_r}}$, $C_{n_{\delta_a}}$, $C_{n_{\delta_r}}$

3.2.1. Formulation of Lift and Pitching Moment coefficients

The steady-state lift coefficient C_L and all derivatives are imported from AVL, and a 4D look-up table with respect to α, β, Mach and Flap Angle are generated. The derivative C_{L_α} implements the empirical Equation 1 [12] as a subsystem in the lift model.

$$C_{L_\alpha} = 2C_{L_{\alpha_h}} \eta_h \bar{V}_h \frac{\mathrm{d}\varepsilon}{\mathrm{d}\alpha} \tag{1}$$

$$\frac{d\varepsilon}{d\alpha} = 4.44 \times \left[\frac{1}{A} - \frac{1}{1+A^{1.7}} \times \frac{10-3\lambda}{7} \times \frac{\left(1-\left|\frac{h_h}{b}\right|\right)}{\sqrt{\frac{2l_h}{b}}} \times \sqrt{\cos \Lambda_{\frac{1}{4}}} \right]^{1.19} \tag{2}$$

where

$C_{L_{\alpha_h}}$ – C_{L_α} of the horizontal stabilizer (Obtained via a look-up table from AVL)

η_h – Tailplane efficiency factor

$\bar{V}_h$ – Tailplane volume factor

$d\varepsilon/d\alpha$ – Rate of change of downwash w.r.t α (Calculated using Equation 2 [10])

h_h – Height of horizontal stabilizer

l_h – Length to horizontal stabilizer

The lift contribution from the elevator is then accounted for by a look-up table of $C_{L_{\delta e}}$ created from AVL output. The final form of the lift model is shown in Figure 6.

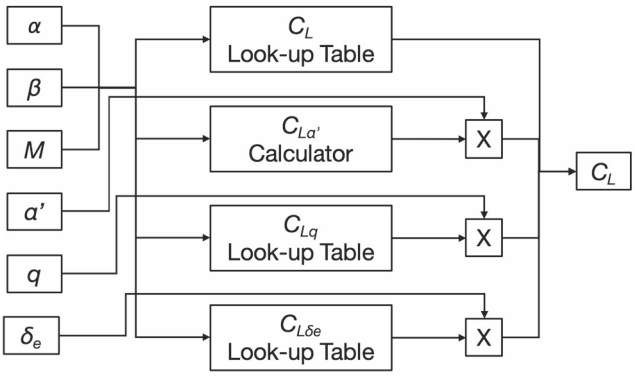

Figure 6. Illustration of the improved lift model.

Similar to the lift model, the majority of pitching moment derivatives are obtained from AVL, while the dynamic derivative C_m is obtained using Equation 3.

$$C_{\dot{m}_\alpha} = -2C_{L_{\alpha_h}} \eta_h \bar{V}_h \left(\overline{x_{ac_h}} - \overline{x_{cg}} \right) \frac{d\varepsilon}{d\alpha} \tag{3}$$

where

$\overline{x_{ac_h}}$ – Normalized position of the aerodynamic center of the horizontal stabilizer

$\overline{x_{cg}}$ – Normalized position of the center of gravity

The final form of the improved pitching moment model is shown in Figure 7.

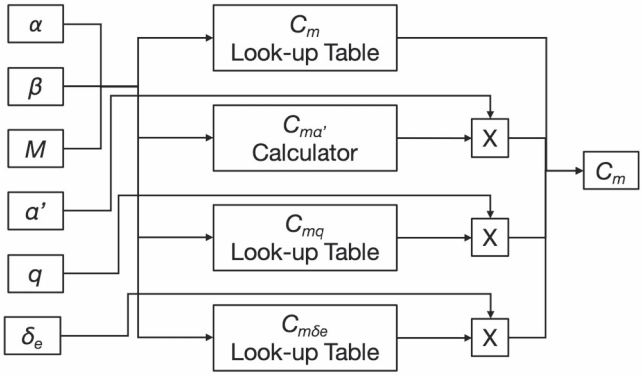

Figure 7. Illustration of the improved pitching moment model.

3.2.1. Drag Model

The total aircraft drag is defined by Equation 4.

$$C_D = C_{D_{min}} + C_{D_i} + C_{D_c} + C_{D_{misc}} \tag{4}$$

where C_{Dmin} is the parasite drag, C_{Di} is the induced drag, C_{Dc} is the compressibility drag, and C_{Dmisc} is the miscellaneous drag. During the simulation, the induced drag component C_{Di} is obtained from AVL, and a look-up table is generated. The performance of the C_{Di} subsystem is assessed in Section 5.1. The compressibility drag is also estimated within AVL via the Prandtl-Glauert compressibility correction and is included within the total inviscid drag.

The parasitic drag exerted on the aircraft is estimated using the component build-up method, which estimates the zero-lift drag of the aircraft by adding up the parasitic drag of each component of the aircraft, the general methodology of which is illustrated in Figure 8. The parasitic drag is described by the superposition of corresponding drag components for each major part of the aircraft, as shown in Equation 5.

$$\sum_{i=1}^{N} C_{D_{min_i}} = \left(\frac{S_{wet_i}}{S_{ref}} \right) C_{f_i} \cdot FF_i \cdot IF_i \tag{5}$$

where C_{fi} represents the skin friction coefficient of the component, FF_i is the form factor, and IF_i is the interference coefficient. To estimate C_f, the Reynolds number must first be determined by the minimum value of Equation 6 [5].

$$\begin{cases} \mathrm{Re} = \dfrac{\rho V l}{\mu} \\ \mathrm{Re}_{cutoff} = 38.21\left(l/k\right)^{1.503} \end{cases} \tag{6}$$

$$\mu = 1.458 \times 10^{-6} T^{1.5} \left(\frac{1}{T + 110.4} \right) \tag{7}$$

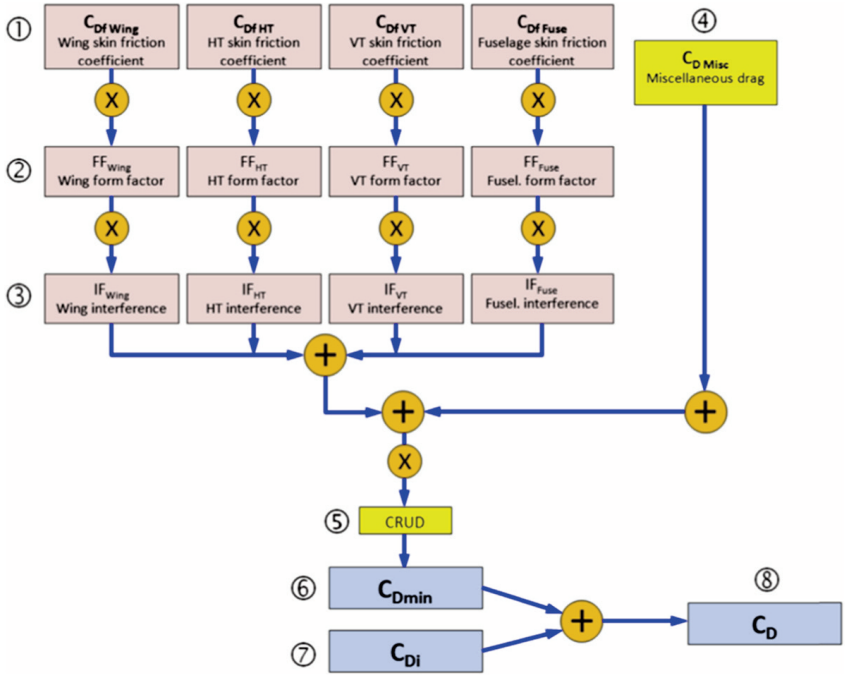

Figure 8. Illustration of the component build-up method to estimate zero-lift drag (C_{Dmin}) [5].

where

ρ	– Density of freestream	(Value provided by ISA Model)
V	– Velocity of freestream	(Depends on flight condition)
l	– Characteristic Length	(Given by the dimensions of each component)
μ	– Dynamic viscosity of air	(Calculated using Equation 7)
k	– Surface roughness value	(Given by values in Table 2)
T	– Outside Air Temperature	(Given by the ISA model)

Table 2. Surface roughness values for different surface materials and finishes [5].

Surface Roughness	$k \times 10^{-5}$ (l **in ft**)
Camouflage paint on aluminum	3.3
Smooth paint	2.08
Production sheet metal	1.33
Polished sheet metal	0.50
Smooth molded composite	0.17

The Reynolds number is then used in the following steps to estimate the value of the skin friction coefficient. This is also the step where the location of the transition point from a laminar to turbulent boundary layer is defined by the user. The location of the fictitious turbulent boundary layer is calculated by the user-defined transition point, X_{tr}, using Equation 8 [5]. The skin friction coefficient is then determined using Equation 9 [5].

$$\left(\frac{X_0}{C}\right) = 36.9 \times \left(\frac{X_{tr}}{C}\right)^{0.625} \left(\frac{1}{\mathrm{Re}}\right)^{0.375} \tag{8}$$

$$C_f = \frac{0.074}{\mathrm{Re}^{0.2}} \left(1 - \left(\frac{X_{tr} - X_0}{l}\right)\right)^{0.8} \tag{9}$$

This method is implemented into Simulink as a sub-model for each component. It should be noted that the C_f of the upper surface and the lower surface of the wing is accounted for separately, and then averaged for the drag estimation over the wing. The wing is treated as four separate spanwise sections such that the position of the transition point along the span of the wing can be varied.

Table 3. X_{tr} setting for each component of the SE2A MRA.

Component	X_{tr}
Inboard Wing Panels	0.70 (Upper Surface), 0.45 (Lower Surface)
Wing Tip	0.60 (Upper Surface), 0.50 (Lower Surface)
Horizontal Stabilizer	0.50 (Upper Surface) [5], 0.50 (Lower Surface) [5]
Vertical Stabilizer	0.30
Fuselage	0.51*

*Fuselage transition point is taken to be the position of the wing-fuselage junction.

Form Factors *FF* for each individual component account for the pressure drag due to varying geometry [10], and are estimated using Equations 10–12 [10].

Wings, empennage or other lifting surfaces [10]:

$$FF_{wing} = \left[1 + \frac{0.6}{(x/c)_{\max}} \left(\frac{t}{c}\right) + 100 \left(\frac{t}{c}\right)^4\right] \times \left[1.34 M^{0.18} \left(\cos \Lambda_{t\max}\right)^{0.28}\right] \tag{10}$$

Fuselage [10]:

$$FF_{fuse} = 1 + \frac{60}{f^3} + \frac{f}{400} \tag{11}$$

Engine nacelles [10]:

$$FF_{nacelle} = 1 + \frac{0.35}{f} \tag{12}$$

where

$(x/c)_{\max}$ – Location of the maximum airfoil thickness

t/c – Thickness-to-chord ratio

$\Lambda_{t\max}$ – Sweep angle of the maximum thickness line

f – Fineness Ratio (Length over diameter $f = l/d = l/\sqrt{4A\max/\pi}$)

Interference Factors IF measure the interference drag between individual components and the fuselage, caused primarily by the merger of the boundary layers of the components with that of the fuselage and the resulting drag [10]. It should be noted that IF can be defined by the user in the MATLAB initializer should the aircraft geometry alter during the design process.

Using the aforementioned methods, with the Swet values provided by Karpuk [8] input into the MATLAB initializer, an estimation of CD0 due to the aircraft components is calculated in real-time as the flight simulation is carried out, and the performance of the CD0 model is tested in Section5.1.

For the miscellaneous drag, two sources are considered in the simulator. Leakage and protuberance drag is the drag caused by high-pressure zones throughout the aircraft, caused by protuberances such as antennas, door edges and hinges [10]. It is difficult to predict by nature, hence it is assumed to contribute a 3% addition to the parasitic drag as shown in Figure 8.

The Cumulative Result of Undesirable Drag (CRUD) represents the undesirable drag exerted on aircraft caused by dirt, misaligned sheet-metal panels etc. [5]. Similar to leakage and protuberance drag, it is accounted for by an arbitrary constant multiplied by the parasitic drag as shown in Figure 8. Gudmundsson [5] advises CRUD to be taken as 1.25 during the preliminary design process, and to adjust the value as the aircraft design progresses through high-fidelity CFD modeling, wind tunnel or flight testing.

3.3. Lateral Force and Moment Model

Lateral stability and control coefficients and derivatives follow a similar approach to longitudinal coefficients. The steady-state coefficients, perturbed-state, and control derivatives are again found via look-up tables generated from AVL. The general layout of the lateral force and moment coefficient model is illustrated in Figure 9.

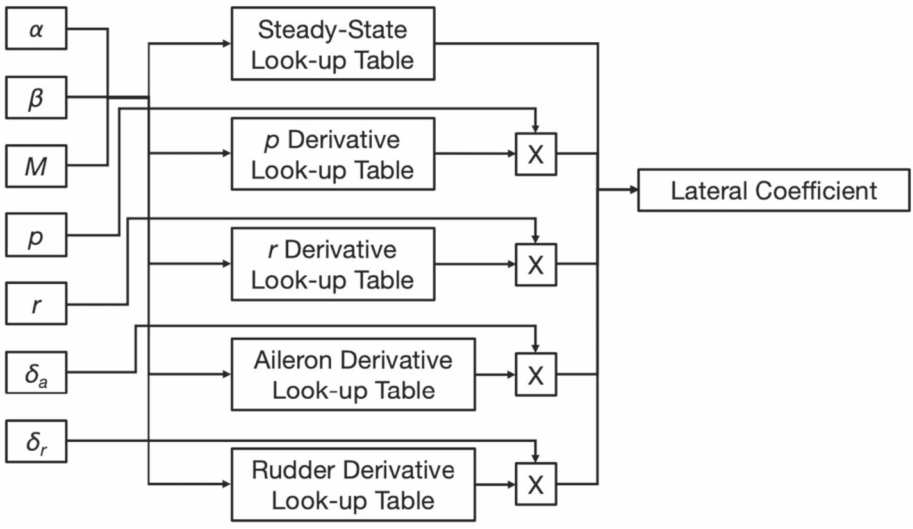

Figure 9. General illustration of the improved lateral force and moment models.

3.4. Development of the High-Lift Device Module

The simulator can mimic the deployment of high-lift devices such as flaps, spoilers, slats and landing gear, and their effects on aircraft performance.

3.4.1. Flap Model

There are two ways to achieve this, either by designing a Simulink sub-model that simulates the effects of different flap designs and settings, or by altering the flap design in AVL, obtaining the look-up tables for aerodynamic force and moment coefficients at different flap settings, and allowing for the option to switch between the different sets of data and tables. The empirical model would have the advantage of requiring less computation to provide a preliminary estimate for the lift and drag generated by different flap designs. Lift generated by different types of flaps is estimated using the method provided by Torenbeek [17]. The lift increment is estimated using Equation 13 [17].

$$\Delta_f C_L = \Delta_f c_{l_0} \left(\frac{C_{L_\alpha}}{c_{l_\alpha}} \right) K_b K_c \tag{13}$$

where

$\Delta_f c_{l_0}$ – Airfoil section lift increment at $\alpha = 0$ due to flap deflection

c_{l_α} – 2D lift curve slope of the airfoil

K_b – Flap span factor

K_c – Flap chord factor

The 2D flap effectiveness parameter, $(\alpha_\delta)_{c_l}$, is required to obtain the value of K_c and is found using Equation 14 [17], where η_δ is the flap lift effectiveness factor and α_δ is the rate of change of zero-lift angle of attack with flap deflection, found using Equation 15 [17].

$$(\alpha_\delta)_{c_l} = \eta_\delta \alpha_\delta \tag{14}$$

$$\alpha_\delta = 1 - \frac{\theta_f - \sin\theta_f}{\pi}, \theta_f = \cos^{-1}\left(2\frac{c_{flapped}}{c} - 1 \right) \tag{15}$$

To consider various types of flaps, K_b, K_c and η_δ look-up tables are integrated into the Simulink model via flap selectors designed using IF-ACTION blocks. The user can enter a value that selects the flap type, and the corresponding look-up tables are selected for use. A schematic of the η_δ selector is shown in Figure 10.

$\Delta_f c_{l_0}$ is calculated using Equation 16 [17], where c_{l_α} is found using a look-up table with data from XFOIL for various Re and Mach numbers, while δ_f is the flap deflection angle.

$$\Delta_f c_{l_0} = \eta_\delta \alpha_\delta c_{l_\alpha} \delta_f = (\alpha_\delta)_{c_l} c_{l_\alpha} \delta_f \tag{16}$$

The Profile Drag generated by the flaps is also estimated using the method provided by Torenbeek [17]. The wing profile drag increment is calculated by Equation 17 [17].

$$\Delta_f C_{D_p} = 1.15 \cdot \frac{S_{W_f}}{S} \cdot \Delta_f c_{d_{p0}} \cdot \cos \Lambda_{1/4} - k_l \cdot c_{d_{p0}} \cdot \Delta_f C_{L_0} \cdot \left[C_L - \left(C_{L_0} + \frac{1}{4} \Delta_f C_{L_0} \right) \right] \quad (17)$$

where

$\Delta_f c_{d_{p0}}$ – Airfoil section profile drag increment at α = 0 due to flap deflection

S_{W_f} – The ratio between the planform covered by the flap and the reference planform

k_l – A quantity given by the drag polar in Equation 18

$c_{d_{p0}}$ – Airfoil section zero-lift profile drag (Found using XFOIL)

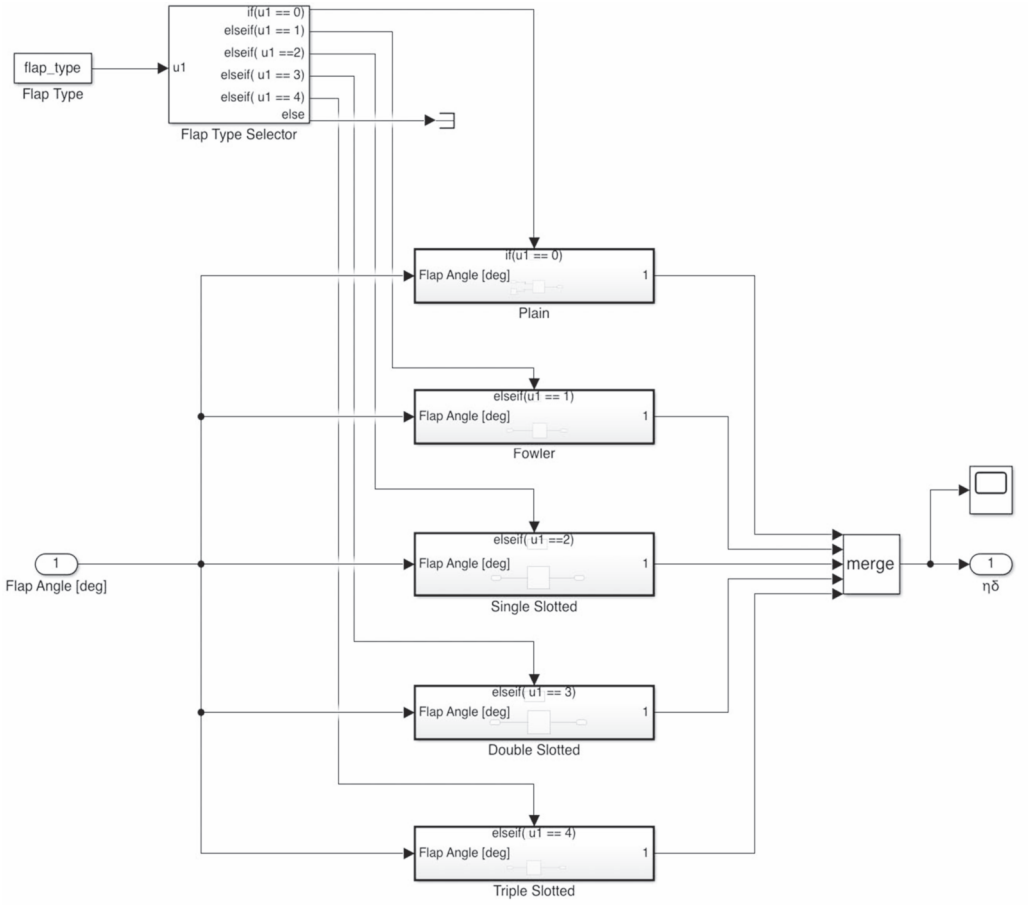

Figure 10. Schematics of the Simulink Flap Selector.

k_l is calculated using the 2D drag polar of the airfoil, which is given by the parabolic Equation 18, and is obtained via a look-up table generated using the drag polar from XFOIL and calculated using MATLAB.

$$c_{d_p} = c_{d_{p0}} \left\{ 1 + k_l \left(c_l - c_l \right)^2 \right\} \quad (18)$$

The airfoil section profile drag increment at α = 0 is found using Equation 19 [17].

$$\Delta_f c_{d_{p0}} = k_d c_{l_\alpha} \alpha_\delta \frac{c_f}{c} \delta_f \sin\delta_f + c_{d_{p0}} \left(\frac{c'}{c} - 1 \right) \tag{19}$$

where

k_d – Parasite drag correction factor obtained from Ref [17]

c'/c – Ratio of extended chord of the airfoil section to flaps retracted

The extended chord factor is found using Equation 20, where c_f/c depends on the flap type and is found in Ref [17]. Again, a flap selector similar to that detailed for η_δ is implemented for c_f/c according to the curves found in Ref [17].

$$\frac{c'}{c} = 1 + \frac{\Delta c}{c_f} \frac{c_f}{c} \tag{20}$$

Induced drag increment due to flap deflection is calculated using Equation 21, where the empirical constant K is found in Ref [17].

$$\Delta_f C_{D_i} = K^2 \left(\Delta_f C_L \right)^2 \cos\Lambda_{c/4} \tag{21}$$

The pitching moment generated by the flaps is estimated using the method described by Roskam [11]. The incremental airplane and wing pitching moment due to flaps, assuming that no canards are present in the design, is given by Equations 22 [11] and 23 [11] respectively.

$$\Delta C_m = \Delta C_{m_{wing}} + C_{L_{\alpha_h}} \eta_h \left(S_h / S \right) \left(\bar{x}_{ac_h} - \bar{x}_{ref} \right) \Delta\varepsilon_f \tag{22}$$

$$\begin{aligned} \Delta C_{m_{wing}} = & \left(\bar{x}_{ref} - \frac{1}{4} \right) \Delta C_{L_{wing}} + K_\Lambda \left(A/1.5 \right) \Delta C_{L_{ref\,wing}} \tan\Lambda_{c/4} \\ & + K_p \left[\left(\Delta C_{m'} / \Delta C_{L_{ref\,wing}} \right) \Delta C_{L_{ref\,wing}} \left(c'/c \right) \right] \\ & - K_p \left\{ \frac{1}{4} \Delta C_{L_{wing}} \left[\left(c'/c \right)^2 - \left(c'/c \right) \right] \right\} \\ & + K_p C_{m_{wing}} \left[\left(c'/c \right)^2 - 1 \right] \end{aligned} \tag{23}$$

where

x_{ref} – Reference point of Cm calculation [11]

x_{ac_h} – Position of horizontal stabilizer aerodynamic center [11]

K_Λ – Swept-wing partial-span flap conversion factor [11]

K_p – Flap span factor [11]

$\Delta C_{m'} / \Delta C_{L_{ref\,wing}}$ – Moment-to-lift ratio [11]

Again, a similar selector to that in the lift and drag model that selects look-up tables for K_Λ, K_p and $\Delta C_{m'} / \Delta C_{L_{ref\,wing}}$ based on flap specifications is implemented.

3.4.2. Spoiler Model

The spoilers are assumed to contribute to drag in the same manner as leakage drag, as a fixed gain of the parasite drag by about 2% as estimated by Sadraey [13]. A switch is added in the control inputs to allow the user to extend or retract the spoilers.

3.4.3. Slat Model

The deployment of leading-edge slats increases stall angle and $C_{L\max}$, as well as the zero-lift drag of the wing. However, since AVL does not generate reliable results at high angles of attack by nature, it would not be useful to simulate the lift-related effects due to the deployment of slats. Hence, only the increase in drag is simulated. The Sadraey method provided in Equation 24 [13] is used to model the increase in zero-lift drag due to the deployment of slats empirically.

$$C_{D_{0,slats}} = \left(\frac{c_{slat}}{c}\right) C_{D_{0,wing}} \tag{24}$$

where c_{slat}/c is the ratio average chord with average extended slat chord to average wing chord, which can be defined by the user in the MATLAB initialization file.

3.4.4. Landing Gear Model

The ability to simulate the drag created by the landing gear is another function that is added to the simulator. A switch is added in the control inputs for the user to extend and retract the landing gear. The Austyn-Mair and Birdsall empirical method [1], shown in Equation 25, is used in this simulator to estimate the drag created by the landing with flaps retracted and fully-deployed, while the drag at flap settings in between is linearly interpolated between the two values.

$$\Delta C_{D_{Gear}} = \begin{cases} \dfrac{5.698\times10^{-4}\cdot m^{0.785}}{S_{ref}} & \text{(Flaps retracted)} \\ \dfrac{3.099\times10^{-4}\cdot m^{0.785}}{S_{ref}} & \text{(Flaps fully deployed)} \end{cases} \tag{25}$$

where m refers to the mass of the aircraft in kg, and S_{ref} is in m^2.

3.5. Propulsion system modeling

The current simulator is capable of simulating a turbofan engine using low-fidelity semi-empirical methods. The sea-level static thrust is defined by the user, while the thrust variation with the airspeed and altitude depends on the thrust lapse model. In general, various types of energy networks of different fidelity will be developed.

3.5.1. Thrust lapse model selection and implementation

During the integration of the turbofan model into the simulator, a trade study among various thrust lapse models was performed. A study of thrust lapse models by Scholz [15], Howe [7], Mattingly [9] and

Bartel et al. [2] were used for the trade study. Scholz [15] provides a basic estimation of thrust lapse that depends on altitude and bypass ratio. The thrust lapse is defined by Equation 26.

$$\frac{T}{T_0} = \left(m_1 \cdot BPR + m_2\right) \cdot h + m_3 \cdot BPR + m_4 \tag{26}$$

where BPR refers to the turbofan engine bypass ratio and h refers to the cruising altitude of the aircraft in km or ft. The values for m_1, m_2, m_3 and m_4 are detailed in Table 4.

Table 4. Coefficients used in the Scholz thrust lapse estimation [15].

Units	m_1	m_2	m_3	m_4
SI	0.0013	-0.0397	-0.0248	0.7125
Imperial	3.962E-7	-1.210E-5	-0.0248	0.7125

Howe [7] represents a step up from Scholz as this method considers the effect of Mach number on thrust lapse in addition to altitude and bypass ratio. The estimation of thrust lapse takes different forms for different turbofan engine bypass ratios in Howe [7]. The thrust lapse for a turbofan bypass ratio of 5 is defined by Equation 27.

$$\frac{T}{T_0} = \left[0.88 - 0.016 \cdot BPR - 0.3M\right]\left(\frac{\rho}{\rho_0}\right)^{0.7} \tag{27}$$

Mattingly [9] has 2 separate methods for estimating the thrust lapse of low and high bypass ratio turbofan engines, of which the latter is relevant to this project. This estimation depends on altitude, Mach number, throttle ratio (TR). The thrust lapse is defined by Equation 28.

$$\frac{T}{T_0} = \begin{cases} \delta_0\left[1 - 0.49\sqrt{M}\right], & \theta_0 \le TR \\ \delta_0\left[1 - 0.49\sqrt{M} - \dfrac{3\left(\theta_0 - TR\right)}{1.5 - M}\right], & \theta_0 > TR \end{cases} \tag{28}$$

for high bypass ratio turbofan engines, where

$$\delta_0 = \frac{p}{p_0}\left(1 + \frac{\gamma - 1}{2}M^2\right)^{\frac{\gamma}{\gamma - 1}} \tag{29}$$

$$\theta_0 = \frac{T}{T_0}\left(1 + \frac{\gamma - 1}{2}M^2\right) \tag{30}$$

Bartel et al. [2] is the most detailed method of all. It depends on altitude, Mach number, and bypass ratio. The thrust lapse is defined by Equation 31.

$$\frac{T}{T_0} = A' - \frac{0.377(1+BPR)}{\sqrt{(1+0.82\cdot BPR)G_0}} Z'M + \left(0.23 + 0.19\sqrt{BPR}\right) X'M^2 \tag{31}$$

where

$$A' = -0.4327\left(\frac{p}{p_0}\right)^2 + 1.3855\frac{p}{p_0} + 0.0472 \tag{32}$$

$$Z' = 0.9106\left(\frac{p}{p_0}\right)^3 - 1.7736\left(\frac{p}{p_0}\right)^2 + 1.8697\frac{p}{p_0} \tag{33}$$

$$X' = 0.1377\left(\frac{p}{p_0}\right)^3 - 0.4374\left(\frac{p}{p_0}\right)^2 + 1.3003\frac{p}{p_0} \tag{34}$$

$$G_0 = 0.0603\cdot BPR + 0.6337 \tag{35}$$

In order to compare the results of these 4 thrust models, the results from the thrust lapse models over altitude and Mach number are plotted in contour plots and shown in Figure 11. A bypass ratio of 5 is taken for this study, as it is the assumed bypass ratio of a typical mid-range aircraft.

The Scholz model will not be considered as it can be seen from Figure 11 that assuming that thrust-lapse remains constant throughout different Mach numbers produces erroneous results that significantly deviate from the other 3 models. From the remaining 3 models, the Mattingly model is then eliminated as it produces much more conservative estimations of the thrust lapse compared to Howe and Bartel et al., both of which produce consistent results.

Of the remaining 2 models, the Bartel et al. model has a more detailed method in using pressure lapse to account for altitude effects on thrust lapse as opposed to the Howe model. Furthermore, the Bartel et al. model produces higher fidelity results at low altitude and Mach region with no thrust lapse at sea level and M = 0, which is a more reasonable result compared to the value around 0.7 predicted by the Howe model. Hence, the Bartel et al. model is chosen as the thrust lapse model used in the simulator going forward.

The thrust lapse calculation is implemented using a look-up table instead of a function to save development and computational time, as it is much more convenient and quicker to develop a look-up table of the thrust lapses using MATLAB as opposed to implementing a thrust lapse calculator directly into Simulink. This does mean that a new look-up table has to be generated every time the engine design undergoes a change in bypass ratio, but this is trivial with the MATLAB thrust lapse look-up table generator developed.

3.5.2. OEI Simulation Capability

The ability to simulate OEI situations in the simulator is important as there are many requirements regarding OEI aircraft performance and handling qualities in FAR part 25 regulations [3]. In order to simulate this, the thrust settings of the engines are decoupled in the simulator to simulate symmetrical (rear engine inoperative) and asymmetrical (wing-mounted engine inoperative) OEI conditions.

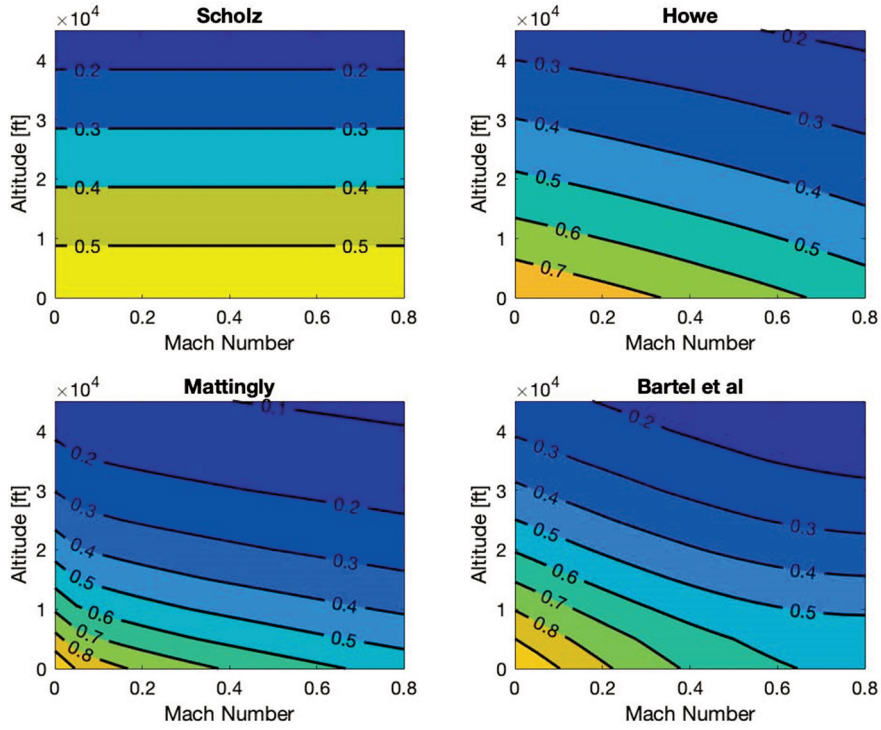

Figure 11. Visualized results from the thrust lapse models at a bypass ratio of 5.

4. SIMULATOR VALIDATION

In order to validate the results produced by the simulator, it is used to simulate an existing airliner. The flight dynamics results are then compared against the flight dynamics characteristics of the airliner. It would be ideal if a modern airliner of a similar payload-range performance could be chosen for the validation exercise, but the Convair CV-880M is chosen in the end as the reference airliner due to data availability.

4.1. Convair CV-880M Model Design

An AVL model of the Convair CV-880M is first designed in order to obtain the look-up tables required. It is initially designed according to the scaled drawings provided in Schmidt [14]. Key specifications of the CV-880M used in the definition of the AVL model are S = 2000.0 ft^2, b = 120.0 ft, c = 18.94 ft and the center of gravity being at 0.195c, provided by Schmidt [14]. Figure 13 shows a model generated using AVL.

The AVL model is then validated at 3 flight conditions to ensure that the data from the model will be as accurate as possible. The validation is carried out by running the AVL model at the 3 flight conditions chosen, which are listed in Table 5. The stability and control derivatives are then extracted from the run data and compared with the literature. Since not all geometric parameters are well-defined, the CV-880M model is correspondingly fine-tuned (e.g., dihedral angle, wing, engine and empennage positioning) to increase the accuracy of the model. This iterative process is carried out until a sufficient level of accuracy is achieved. The stability and control derivatives of the final iteration of the CV-880M

model is shown in Table 6. However, a few outlying values still exist that have converged or proved to be very difficult to fine tune or would sacrifice the accuracy of other derivatives once adjusted. Hence, they are allowed into the final CV-880M model. These values are underlined in Table 6.

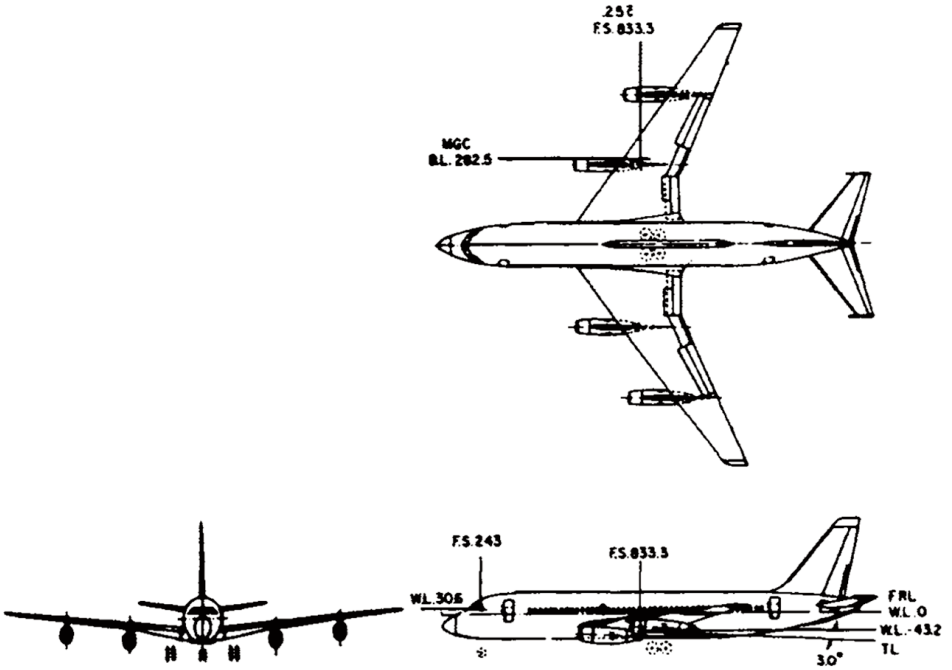

Figure 12. Drawing of the Convair CV-880M [14].

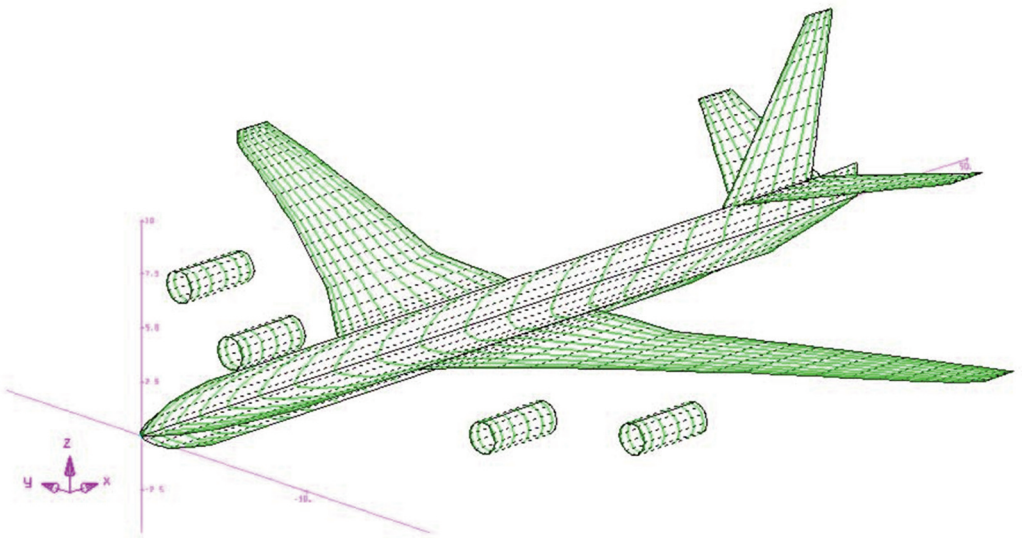

Figure 13. AVL model of the Convair CV-880M.

Table 5. Tested Flight Conditions of the Convair CV-880M [14].

Condition	Landing	Take-Off	Holding	Cruise
h [ft]	0 (S/L)	0 (S/L)	23,000	35,000
M	0.203	0.249	0.86	0.86
V [ft/s]	227	278	881	837
W [lb]	126,000	126,000	155,000	155,000
I_x [slug ft2]	1.170E+6	1.164E+6	1.516E+6	1.523E+6
I_y [slug ft2]	2.450E+6	2.450E+6	2.510E+6	2.510E+6
I_z [slug ft2]	3.570E+6	3.576E+5	4.094E+6	4.087E+6
I_{xz} [slug ft2]	-2.202E+5	-1.833E+5	-1.264E+5	-1.820E+5
δ_{flap} [deg]	50	35	0	0

In general, it is observed that the AVL model is more reliable in the holding and cruise (flaps 0) configurations over the landing (full flaps) configuration. It is expected that this phenomenon will carry through to the results during validation.

Table 6. Stability and Control derivatives of the Convair CV-880M AVL model compared against the literature [14].

Metric	Landing		Take-Off		Holding		Cruise	
	Lit.	AVL	Lit.	AVL	Lit.	AVL	Lit.	AVL
C_{L_α}	4.66	5.210	4.53	5.25	4.8	5.75	4.9	5.32
C_{m_α}	-0.381	-0.326	-0.904	-0.81	-0.571	-0.53	-0.74	-0.73
C_{m_q}	-12.2	-16.121	-12.1	-16.27	-11.81	-16.16	-12.01	-16.75
C_{l_β}	-0.239	-0.557	-0.197	-0.33	-0.144	-0.14	-0.179	-0.18
C_{l_p}	-0.394	-0.504	-0.382	-0.48	-0.244	-0.30	-0.294	-0.36
C_{l_r}	0.308	0.384	0.2	0.21	0.088	0.07	0.146	0.13
C_{Y_β}	-1.011	-0.662	-0.878	-0.68	-0.813	-0.74	-0.842	-0.74
C_{n_β}	0.145	0.099	0.14	0.12	0.122	0.12	0.133	0.12
C_{n_p}	-0.087	-0.133	-0.049	-0.06	-0.003	0.00	-0.005	-0.02
C_{n_r}	-0.218	-0.202	-0.185	-0.19	-0.189	-0.21	-0.165	-0.17
$C_{L_{\delta_e}}$	0.16	0.132	0.153	0.13	0.112	0.10	0.144	0.15
$C_{m_{\delta_e}}$	-0.47	-0.354	-0.456	-0.35	-0.349	-0.27	-0.423	-0.41
$C_{l_{\delta_a}}$	0.0958	0.065	0.0763	0.05	0.0413	0.03	0.0485	0.05
$C_{l_{\delta_r}}$	0.021	-0.012	0.023	0.00	0.018	0.01	0.019	0.01
$C_{Y_{\delta_r}}$	0.223	0.181	0.216	0.18	0.139	0.12	0.169	0.16
$C_{n_{\delta_a}}$	0.02	0.004	0.007	0.00	0.007	0.00	0.006	0.00
$C_{n_{\delta_r}}$	-0.099	-0.079	-0.096	-0.08	-0.053	-0.04	-0.064	-0.06

4.2. Validation against Convair CV-880M Flight Dynamics Data

With the development of the CV-880M AVL model complete, the look-up tables containing the aerodynamic force and moment coefficients, as well as the stability and control derivatives required for the operation of the simulator are obtained using the same method as outlined in the previous section. After performing the simulations, the damping ratio and frequencies of the Short-Period Pitch Oscillation (SPPO), phugoid and Dutch roll modes are obtained. The results are validated by comparing them with the literature values provided in Schmidt [14]. This is shown in Table 7, with the values with large errors underlined.

Table 7. Flight simulation results of the AVL simulator compared against literature [14].

Mode	Eigenvalue	Landing		Take-Off		Holding		Cruise	
		Lit.	AVL	Lit.	AVL	Lit.	AVL	Lit.	AVL
SPPO	ζ	0.794	0.248	0.6	0.341	0.493	0.407	0.381	0.279
	ω [rad s^{-1}]	0.821	1.085	1.291	1.243	2.13	1.287	1.782	1.201
Phugoid	ζ	0.085	0.100	0.059	0.163	0.077	0.335	0.049	0.018
	ω [rad s^{-1}]	0.149	0.205	0.145	0.147	0.049	0.031	0.053	0.169
Dutch Roll	ζ	0.118	0.498	0.136	0.367	0.133	0.157	0.094	0.105
	ω [rad s^{-1}]	1.021	0.669	1.113	0.391	1.879	0.090	1.539	0.071

In general, the AVL results are accurate in terms of the signage and order of magnitude of values, which show the value of the simulator as a tool to assist the flight dynamics analysis of aircraft at the conceptual design stage, though it should be noted that the accuracy of the results decreases as flaps are deployed, most likely due to inaccuracies associated with empirical methods in estimating the aerodynamic effects due to flap deployment. It is seen that the largest errors are present in the eigenvalues produced by the AVL simulator for the Dutch roll mode. This should be due to geometric inaccuracies in the construction of the CV-880M AVL model as the geometric data available for the CV-880M is limited, and lateral stability derivatives are much more sensitive to minor geometric changes compared to longitudinal stability derivatives. This problem should be mitigated for newly designed conceptual aircraft as there will be complete and exact sets of geometric data.

5. EXAMPLE CASE: A MID-RANGE AIRCRAFT

The example case study is the SE2A mid-range commercial aircraft with design mission requirements and payload similar to an Airbus A320 [8]. Figure 14 shows the aircraft geometry while the basic characteristics of the aircraft are presented in Table 8.

In addition, multiple technology assumptions were considered for this aircraft, which are being developed within the cluster. All the technology assumptions used for this aircraft are summarized in Table 9. At the current design stage, technology assumptions are considered as constant correction factors for aerodynamics, weights, and fuel consumption.

Figure 14. SE2A MRA aircraft geometry [8].

Table 8. SE2A MRA specifications [8].

Parameter	**Value**
AR	16.40
λ	0.28
C_r [ft]	15.95
W_0 [lb]	153,653
W_f [lb]	19,266
W_e [lb]	41,334
T/W	2.267

Table 9. SE2A MRA technology assumptions.

Technology	**Assumptions**
Laminar Flow Control	Wing: Laminar flow of 70% chord until the wing folding Fuselage: Laminar flow until the wing-body fairing
Load Alleviation	Limit load factor of 2.0
Advanced Structures	19% reduction of the airframe weight
Boundary Layer Ingestion	5% reduction in specific fuel consumption
Ultra-High Bypass Ratio Turbofan	25% reduction in specific fuel consumption

5.1. Aerodynamic performance simulation using the flight simulator

The performance of the lift model is assessed by simulating the SE2A MRA in trimmed steady-level flight at various altitudes [ft], true air speeds [knots] and Mach numbers post-development of the simulator. The results are shown in Figures 14 and 15, and are deemed reasonable as it is expected that C_L would increase as speed decreases and as altitude increases (air pressure decreases) to maintain the same amount of lift. It is noted in Figures 15 and 16 that C_L values excess of 1.2 are unrealistic, and only serve to illustrate the capabilities of the lift model.

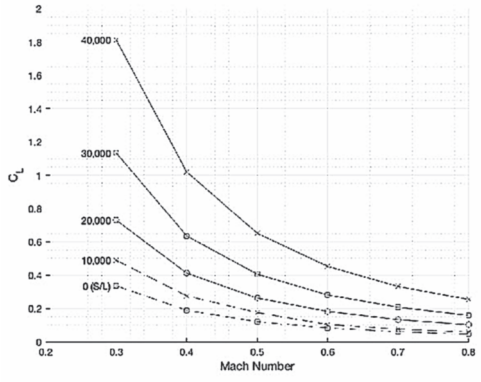

Figure 15. C_L versus Mach Number in SLF.

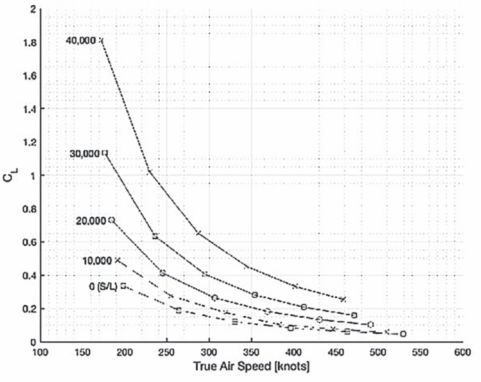

Figure 16. C_L versus TAS in SLF.

The performance of the drag model is assessed post-development of the simulator, at the same trimmed steady-level cruising flight conditions at various altitudes [ft], true air speeds [knots] and Mach numbers as those in Section 3.2.1. The CD results, as well as breakdowns of C_{D0} and C_{D_i} are shown in Figures 17–22. Similar to the performance testing of the lift model, it is noted that C_D values above 0.05 are usually unrealistic and serve only to illustrate the performance of the induced drag model.

After validating the simulator, the simulation of the SE2A MRA can be performed with a higher level of confidence. The static and dynamic stability, and the handling qualities of the SE2A MRA are assessed by comparison to the Convair CV-880M.

5.2. Static Stability Analysis

Overall, the SE2A MRA is statically stable as seen in Table 10. Since the SE2A MRA utilizes a forward-swept wing configuration, it is expected that it would be less statically stable in the lateral modes. It is seen that the C_{Y_β}, C_{l_β} and C_{n_β} performance is indeed weaker than that of an aircraft with a more conventional backwards-swept wing configuration like that of the Convair CV-880M. The C_{Y_β} and C_{l_β} performance of the SE2A MRA is approximately half that of the CV-880M, which suggests that the 4-degree dihedral [8] that the SE2A MRA currently has may not be sufficient for ideal lateral static stability. Furthermore, the C_{n_β} performance is considerably weaker at around one magnitude lower than that of the CV-880M, which could be strengthened by increasing the vertical fin size. Another point of interest is the large C_{m_q} of the SE2A MRA compared to that of the CV-880, and may result in a high frequency in the SPPO dynamic mode.

The other aerodynamic derivatives, as well as the control derivatives of the SE2A MRA, are at the same magnitude and signage as that of the CV-880M. This does not necessarily mean that the control surfaces are adequately sized for the SE2A MRA, since other factors such as damping ratios and inertia play a role in the determination of control surface size. As such, a more detailed control surface sizing assessment should be performed in the future development of the SE2A MRA.

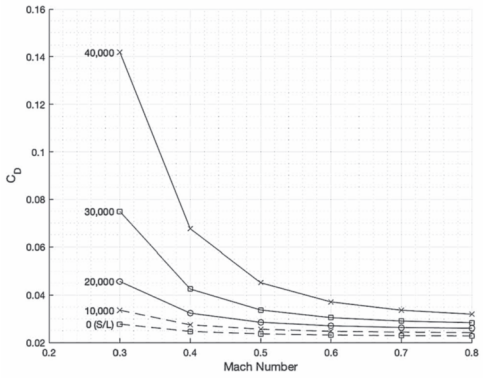

Figure 17. C_D versus Mach Number in SLF.

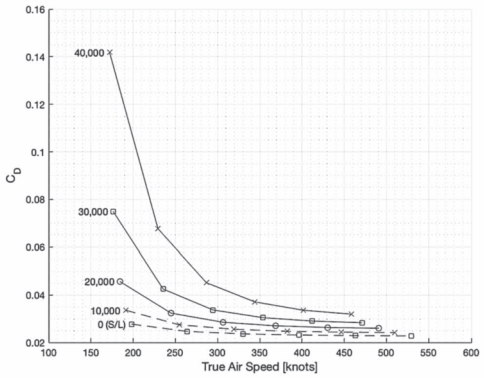

Figure 18. C_D versus TAS in SLF.

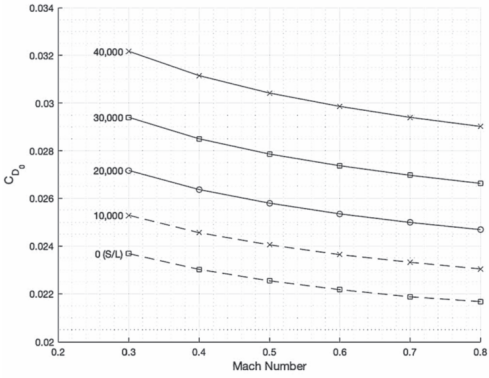

Figure 19. C_{D_0} versus Mach Number in SLF.

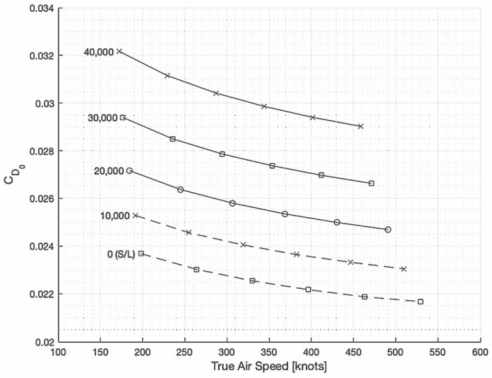

Figure 20. C_{D_0} versus TAS in SLF.

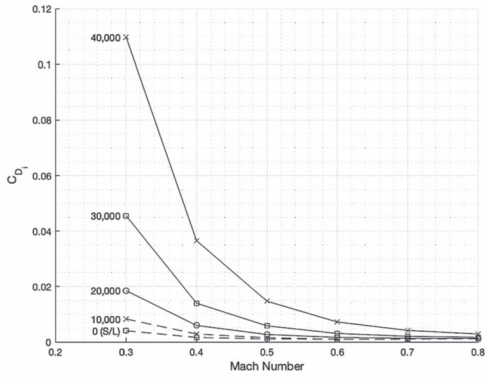

Figure 21. C_{D_i} versus Mach Number in SLF.

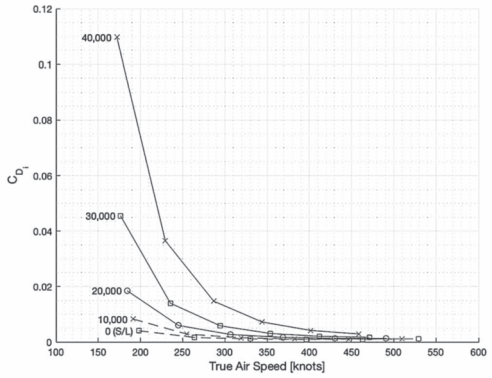

Figure 22. C_{D_i} versus TAS in SLF.

Table 10. Aerodynamic force and moment coefficients and derivatives of the SE2A MRA compared to the Convair CV-880M [14].

	SE2A MRA (from AVL)				**Convair CV-880M (Literature)**			
Flight Segments	Landing	Take-Off	Holding	Cruise	Landing	Take-Off	Holding	Cruise
Mach Numbers	0.25	0.3	0.425	0.78	0.203	0.249	0.86	0.86
Altitude [ft]	0	0	14,000	35,000	0	0	23,000	35,000
TAS [ft/s]	280	335	450	760	227	278	881	837
Flaps [deg]	30	15	0	0	50	35	0	0
C_{L_α}	5.656	5.721	5.756	7.058	4.66	4.53	4.41	4.90
C_{m_α}	-1.612	-1.644	-1.835	-2.127	-0.381	-0.904	-0.571	-0.740
C_{mq}	-30.394	-30.623	-33.342	-39.380	-12.20	-12.10	-11.81	-12.01
C_{Y_β}	-0.427	-0.425	-0.416	-0.447	-1.011	-0.878	-0.813	-0.842
C_{l_β}	-0.068	-0.073	-0.086	-0.098	-0.239	-0.197	-0.144	-0.179
C_{l_p}	-0.499	-0.504	-0.505	-0.596	-0.394	-0.382	-0.244	-0.294
C_{l_r}	0.172	0.155	0.102	0.119	0.308	0.200	0.088	0.146
C_{n_β}	0.014	0.014	0.015	0.023	0.145	0.140	0.122	0.133
C_{np}	-0.031	-0.026	-0.012	-0.017	-0.087	-0.049	-0.003	-0.005
C_{n_r}	-0.136	-0.135	-0.131	-0.142	-0.218	-0.185	-0.189	-0.165
$C_{L_{\delta e}}$	0.414	0.417	0.433	0.523	0.160	0.153	0.112	0.144
$C_{m_{\delta e}}$	-1.537	-1.550	-1.664	-2.032	-0.470	-0.456	-0.349	-0.423
$C_{Y_{\delta r}}$	0.225	0.226	0.222	0.252	0.223	0.216	0.139	0.169
$C_{l_{\delta a}}$	0.076	0.077	0.079	0.095	0.0958	0.0763	0.0413	0.0485
$C_{l_{\delta r}}$	0.032	0.032	0.032	0.038	0.021	0.023	0.018	0.019
$C_{n_{\delta a}}$	0.003	0.002	0.002	0.003	0.020	0.007	0.007	0.006
$C_{n_{\delta r}}$	-0.086	-0.086	-0.086	-0.098	-0.099	-0.096	-0.053	-0.064

5.3. Dynamic Stability and Handling Quality Analysis

The dynamic stability of the SE2A MRA is assessed by first comparing its damping ratio, frequency and reduced frequency of the SPPO, phugoid and Dutch roll to that of the Convair CV-880M. The metrics are then checked against FAR Part 25 [3] and MIL-F-8785C [18] to ensure the SE2A MRA complies with current aircraft regulations.

The damping ratio and frequency of the modes are obtained using the Model Linearizer app in Simulink, which reduces the time required and potential human errors in manually simulating the aircraft. The results are listed in Table 11 along with the corresponding data for the CV-880M as a comparison. The reduced frequency (denoted as k) is calculated using Equation 36.

$$k = \frac{1}{2}\frac{\omega_c}{V_\infty} \tag{36}$$

From Table 11, it can be seen that the SE2A MRA is relatively weakly damped in SPPO, resulting in a higher frequency compared to that of the Convair CV-880M, as predicted from the static stability analysis. The phugoid performance of the SE2A MRA is comparable to the CV-880M. Lastly, the SE2A MRA is more highly damped in Dutch roll compared to the CV-880M.

How the dynamic stability performance of the SE2A MRA compared to that of one counterpart only serves as a reference, as it alone does not determine whether a new aircraft is judged to be safe and fit-to-fly. To perform a more detailed analysis of the dynamic stability performance of the SE2A MRA, its dynamic stability performance is checked to see whether it complies with that outlined in FAR Part 25 [3], as well as regulations in MIL-F-8785C [18] as sound design practice.

Table 11. Dynamic stability data of the SE2A MRA compared to that of the Convair CV-880M [14].

		SE2A MRA (from AVL)				**Convair CV-880M (Literature)**			
Flight Segment		Landing	Take-Off	Holding	Cruise	Approach	Take-Off	Holding	Cruise
Mach Number		0.25	0.3	0.425	0.78	0.203	0.249	0.86	0.86
SPPO	ζ	0.1790	0.2020	0.1450	0.1110	0.794	0.600	0.493	0.381
	ω [rad s^{-1}]	5.8500	7.1800	7.6100	9.8400	0.821	1.291	2.130	1.782
	k	0.0978	0.1003	0.0792	0.0606	0.0343	0.0440	0.0229	0.0202
Phugoid	ζ	0.0314	0.0640	0.1850	0.1350	0.085	0.059	0.077	0.049
	ω [rad s^{-1}]	0.0237	0.0251	0.0184	0.0163	0.149	0.145	0.049	0.053
	k	0.0004	0.0004	0.0002	0.0001	0.0062	0.0049	0.0005	0.0006
Dutch Roll	ζ	0.4060	0.4360	0.4490	0.3490	0.118	0.136	0.133	0.094
	ω [rad s^{-1}]	0.7180	0.7770	0.5250	0.6510	1.021	1.113	1.879	1.539
	k	0.0120	0.0109	0.0055	0.0040	0.0426	0.0379	0.0202	0.0174

Before proceeding, it is important to collate the definitions required for compliance analysis. The SE2A MRA is defined as a Class II 'Medium weight, low-to-medium maneuverability' aircraft in MIL-F-8785C [18], which is the military equivalent to FAR Part 25 aircraft. The mission profile of the SE2A MRA is entirely confined within Category B and C flight phases defined in MIL-F-8785C, as outlined in Table 12.

Table 12. Definitions of the relevant flight phase categories according to MIL-F-8785C [18].

Category	**Definition**	**Examples**
B	Those non-terminal flight phases that are normally accomplished using gradual maneuvers and without precision tracking, although accurate flight-path control may be required.	Climb, Cruise, Loiter, Descent
C	Terminal flight phases are normally accomplished using gradual maneuvers and usually require accurate flight path control.	Take-Off, Approach, Landing

The flying qualities required of an aircraft vary by flight phase. MIL-F-8785C presents 3 flying quality levels, and these are listed in decreasing order of desirability in Table 13.

Table 13. Flying Quality Levels as outlined in MIL-F-8785C [18].

Level	**Definition**
1	Flying qualities clearly adequate for the mission Flight Phase.
2	Flying qualities adequate to accomplish the mission Flight Phase, but some increase in pilot workload or degradation in mission effectiveness, or both, exists.
3	Flying qualities such that the airplane can be controlled safely, but pilot workload is excessive or mission effectiveness is inadequate, or both. Category B and C Flight Phases can be completed.

The compliance of the SE2A MRA is then analyzed using both FAR Part 25 [3] and MIL-F-8785C [18] in Table 14.

Table 14. Compliance analysis of the dynamic stability characteristics of the SE2A MRA [3] [18].

Performance Metric	**Source**	**Compliance Condition**	**Proof of (Non-)Compliance**	**Status**
Phugoid Damping Ratio	FAR Part 25	No requirement.	N/A	N/A
	MIL-F-8785C	$\zeta \geq 0$.	$\zeta > 0$ at all tested flight segments.	Compliant
SPPO Natural Frequency	FAR Part 25	No specific limits.	N/A	N/A
	MIL-F-8785C	Refer to Figure 23.	Table shows that SPPO natural frequencies at all flight segments are confined in the highest flying quality Level 1 in Figure 22.	Marginally Compliant
SPPO Damping Ratio	FAR Part 25	Must be heavily damped.	ζ of SE2A MRA at all flight segments are significantly weaker than that of the CV-880M, hence not considered to be 'heavily damped'.	Non-Compliant
	MIL-F-8785C	Refer to Table 16.	ζ does not meet the requirements for Category B flight phase, while only meeting the lowest Level 3 flying quality requirements for Category C flight phase.	Non-Compliant
Dutch Roll Natural Frequency	FAR Part 25	No requirement.	N/A	N/A
	MIL-F-8785C	Refer to Table 17.	ω at all flight segments are larger. than the minimum requirement.	Compliant
Dutch Roll Damping Ratio	FAR Part 25	$\zeta > 0$ with controls.	$\zeta > 0$ at all tested flight segments.	Compliant
	MIL-F-8785C	Refer to Table 17.	ζ at all flight segments are larger than the minimum requirement.	Compliant

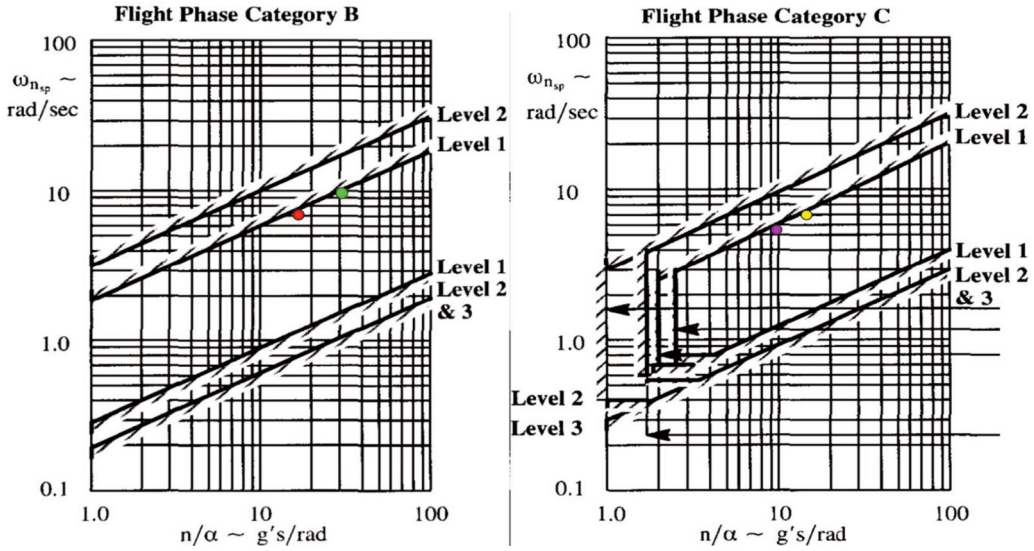

Figure 23. SPPO Natural Damping Frequencies of the SE2A MRA
(Red – Holding; Green – Cruise; Magenta – Landing; Yellow – Take-Off) [18].

The quantity n/α used in Figure 23 is found by Equation 37 [18].

Table 15. n/α for different flight segments of the SE2A MRA.

Flight Segment	Landing	Take-Off	Holding	Cruise
Flight Phase Category	C	C	B	B
$\boldsymbol{n/\alpha}$	9.82	14.23	16.86	30.49
$\boldsymbol{\omega}$	5.85	7.18	7.61	9.84

From Table 14, it can be seen that the dynamic stability characteristics of the SE2A MRA are compliant with both FAR Part 25 [3] and MIL-F-8785C [18] apart from the SPPO damping ratio requirements, where the damping ratios are too low for the aircraft to have acceptable flying qualities.

Table 16. SPPO Damping Ratio requirements for Category A, B and C flight phases [18].

Flying Quality Level	**Category A and C**		**Category B**	
	Min.	**Max.**	**Min.**	**Max.**
1	0.35	1.30	0.30	2.00
2	0.25	2.00	0.20	2.00
3	0.15	No Max	0.15	No Max

Table 17. Dutch roll damping ratio and natural frequency requirements at different flying qualities [18].

Flying Quality Level	Minimum ζ	Minimum ω
1	0.08	0.4
2	0.02	0.4
3	0	0.4

5.4. Responsiveness Assessment

The responsiveness of the SE2A MRA is assessed by observing the p, q and r behavior over time when adding an impulse to the aileron, elevator and rudder respectively at different flight segments and configurations, and then comparing this behavior to that of the Convair CV-880M. The p, q and r of the Convair are obtained by designing a MATLAB code that takes the aircraft parameters and body-axes dimensional derivatives from Heffley [6] and solves the eigenvalue problem of the equations of motion of aircraft. The same initial impulse loads are then exerted onto the CV-880M to simulate the motion of the aircraft for comparison with the SE2A MRA.

From Figure 24, it can be seen that the p and r behaviors of the 2 aircraft display a similar trend, with the yaw rate of the Convair CV-880M having a slightly shorter period than that of the SE2A MRA. This shows that the SE2A MRA has acceptable aileron and rudder responsiveness, as well as acceptable p and r behaviors.

However, the q responses of the two aircraft differ substantially, with the response of the SE2A MRA having a much shorter period than that of the CV-880M. This is expected from the highly negative value of Cmq seen during the static stability analysis, as well as from the low ζ and high ω of the SPPO mode seen during the dynamic stability analysis.

5.5. Requirements for the next design stage

To summarize, there are 2 areas in which the SE2A MRA requires improvement before progressing to the next stage of design.

The first refinement of the aircraft concept would be to increase the lateral stability of β-derivatives. As mentioned in the static stability analysis, forward-swept wing designs tend to be weak in β-derivatives. While the current 4-degree dihedral that the SE2A MRA has is enough to make it statically stable, it is still not as stable as conventional backwards-swept wing designs. This may be an issue down the line as it could cause accidents from control unfamiliarity of pilots, as is the case with many forward-swept wing aircraft such as the HFB 320 Hansa Jet and the V-22 Osprey. Increasing the wing dihedral and vertical fin size could solve these issues if the aircraft structure permits. Alternatively, $p-\beta$ flight control laws could be implemented to augment an increase in lateral stability.

The second refinement would be to increase the damping ratio and reduce the frequency of the SPPO dynamic mode. This is a more pressing issue as the SPPO damping ratio and frequency of the SE2A MRA do not comply with FAR Part 25 nor MIL-F-8785C regulations. In addition, the C_{m_q} and q-response of the SE2A MRA differ substantially from that of the existing aircraft example. Since damping in the SPPO mode is dominated by C_{m_q}, the recommendation would be to increase the value of C_{m_q}. If the structure permits, this could be done by increasing the length of the aft section of the fuselage, and hence the horizontal stabilizer moment arm, or by increasing the horizontal stabilizer area. Alternatively, pitch rate feedback controllers could again be installed to augment a higher value of C_{m_q}.

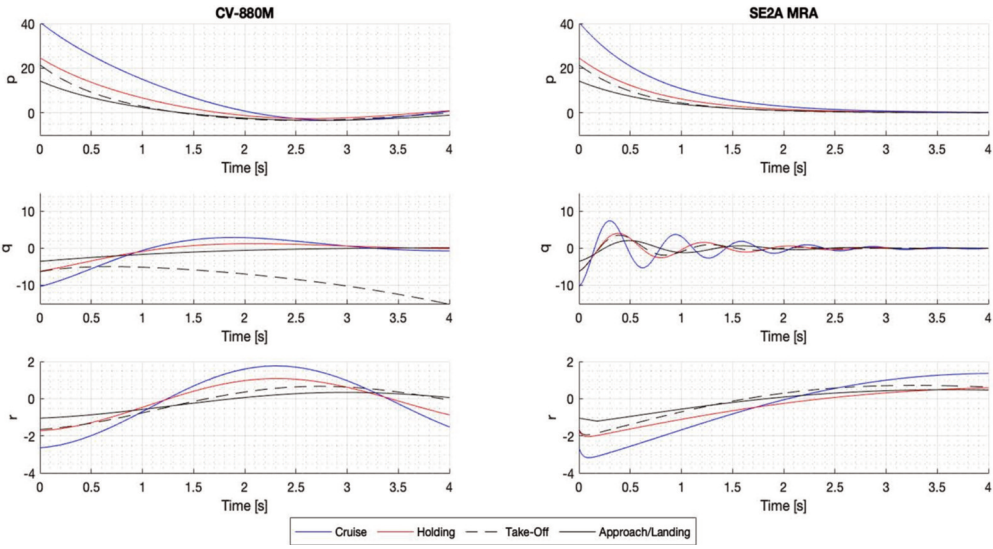

Figure 24. *p*, *q* and *r* responses of the SE2A MRA compared to that of the Convair CV-880M.

6. DISCUSSION

Limitations of the delivered simulator at its current stage of development are:

1. **Inability to simulate long flight segments** as there is no fuel consumption and fuel mass variation model present in the simulator. This is not a problem for point-performance analysis such as that performed above, but the absence of fuel consumption and fuel mass variation models will not allow for proper range and endurance simulations and analysis of conceptual aircraft;
2. **Limited engine type selection** as the simulator only allows for the selection of turbofan engines. For future projects, more types of engines and modes of propulsion available for selection would be desired, such as turboprop engines, propfans, distributed propulsion systems and engines that rely on electricity or alternative fuels;
3. **Lack of consideration of aeroelasticity and load alleviation systems** since the simulator uses a rigid aircraft assumption. It is recommended that the simulation of wing loading be added as a feature in the simulator for future projects since it is critical to simulate the structural loading on wings designed using new technologies, systems, and materials. Aeroelasticity should also be modeled in the future as it has a non-negligible effect on aircraft performance, particularly for high aspect ratio, lightweight wings;
4. **Lack of visual interfaces** makes it difficult to understand the maneuvers that the aircraft is experiencing, as this is not immediately intuitive from the mere observation of Simulink scopes. It is recommended that the output of the simulation be processed by software such as FlightGear to provide a more user-friendly experience.

7. CONCLUSION

The project has been conducted since a highly customizable flight simulator is needed in the SE2A research cluster for novel aircraft conceptual design. The key features and methodologies of the simulator include:

1. The usage of look-up tables for aerodynamic force and moment coefficients and derivatives obtained using AVL to avoid using fixed gains to calculate for the same quantities under different atmospheric conditions;
2. Development of a sophisticated drag model that uses lookup tables from AVL for C_{D_i} estimations, and calculates C_{D_0} in real-time during simulation, depending on parameters such as aircraft geometry, laminar-to-turbulent transition point and Reynolds numbers experienced by individual components;
3. Development of a thrust model that considers thrust lapse due to the effects of altitude and Mach number;
4. A flap model that utilizes empirical textbook methods to predict the effect of different flap designs on the aerodynamic coefficients, and hence aircraft performance.

The developed simulator is then scrutinized through a validation process. An AVL model of the Convair CV-880M is created and used to produce data for the simulator. The CV-880M dynamic stability results from the simulator are then compared against the literature values provided in Schmidt [14]. Results show that the simulator is generally accurate, and errors present are most likely due to an inexact CV-880M AVL model and inaccuracies in AVL itself.

The simulator proceeds to simulate the SE2A MRA to provide preliminary static stability, dynamic stability and handling qualities assessment to ensure that the aircraft complies with FAR Part 25 and MIL-F-8785C regulations before proceeding to the next design stage. Results show that while the SE2A MRA is statically and dynamically stable in all flight segments, performs well in roll rate and yaw rate and has good aileron and rudder responsiveness, it has a relatively weak performance in the β-direction and a non-compliant performance in the SPPO dynamic mode. Hence, the following 2 design recommendations are made for the SE2A MRA to address the aforementioned issues:

1. An increase in the positive dihedral of the wing;
2. An increase in C_{m_q} performance, either by increasing the length of the horizontal stabilizer moment arm, or by increasing the horizontal stabilizer area.

If the aircraft structure does not permit the design changes in any case, it is recommended that relevant feedback controllers be installed to augment a higher level of stability.

Some limitations of the simulator are identified, and future work could be focused on addressing its current limitations.

Acknowledgments: We would like to acknowledge the funding by the Deutsche Forschungsgemeinschaft (DFG, German Research Foundation) under Germany's Excellence Strategy—EXC 2163/1-Sustainable and Energy Efficient Aviation—Project-ID 390881007.

REFERENCES

[1] Austyn-Mair, W. and Birdsall, David L. *Aircraft Performance*. 1st ed. Vol. 5. Cambridge Aerospace Series. Cambridge University Press. Cambridge, United Kingdom (1992). ISBN: 0521568366.

[2] Bartel, Matthias and Young, Trevor. "Simplified Thrust and Fuel Consumption Models for Modern Two-Shaft Turbofan Engines." *Journal of Aircraft* J AIRCRAFT 45 (July 2008), pp. 1450–1456. DOI: 10.2514/1.35589.

[3] Department of Transportation Federal Aviation Administration. "Electronic Code of Federal Regulations Title 14 Part 25." Online. Airworthiness Standards: Transport Category Airplanes. Washington DC. (2016).

[4] "Flightpath 2050: Europe's Vision for Aviation." European Commission, Luxembourg. (2011). ISBN: 9789279197246.
[5] Gudmundsson, Snorri. *General Aviation Aircraft Design: Applied Methods and Procedures.* 1st ed. Elsevier Inc, Oxford UK (2014). ISBN: 9780123973085.
[6] Heffley, R. K. and Jewell, W. F. "Aircraft handling qualities data." Tech. rep. NASA CR-2144. National Aeronautics and Space Administration. Washington D.C. (1972).
[7] Howe, Denis. *Aircraft Conceptual Design Synthesis.* Vol. 5. Aerospace Series. Wiley (2000). ISBN: 9781860583018.
[8] Karpuk, Stanislav and Elham, Ali. "Conceptual Design Trade Study for an Energy-Efficient Mid-Range Aircraft with Novel Technologies". *AIAA Scitech.* (2021). DOI: 10.2514/6.2021-0013.
[9] Mattingly, Jack D. *Aircraft Engine Design.* AIAA Education Series. American Institute of Aeronautics and Astronautics, Inc. (2018). ISBN: 978162 4105173.
[10] Raymer, Daniel P. *Aircraft Design: A Conceptual Approach.* 6th ed. AIAA Education Series. American Institute of Aeronautics and Astronautics, Inc. Virginia, U.S.A. (2018). ISBN: 9781624104909.
[11] Roskam, Jan. *Airplane Design Part VI: Preliminary Calculation of Aerodynamic, Thrust and Power Characteristics*. Design, Analysis and Research Corporation. Kansas, U.S.A: (2004). ISBN: 1884885527.
[12] Roskam, Jan. *Airplane Flight Dynamics and Automatic Flight Controls.* 1st ed. Vol. 1. Design, Analysis and Research Corporation. Kansas, U.S.A. (1995). ISBN: 1884885179.
[13] Sadraey, Mohammad H. *Aircraft Performance: An engineering approach.* CRC Press, FL (2016). ISBN: 9781498776554.
[14] Schmidt, Louis V. *Introduction to Aircraft Flight Dynamics. Vol. 1.* American Institute of Aeronautics and Astronautics, Inc. VA, USA. (1998). ISBN: 1563472260.
[15] Scholtz, Dieter. *Aircraft design notes: 5. preliminary sizing*. (2015) https://www.fzt.haw-hamburg.de/pers/Scholz/HOOU/AircraftDesign_5_PreliminarySizing.pdf
[16] Lukaczyk, Trent W., Wendorff, Andrew D., Colonno, Michael, Economon, Thomas D., Alonso, Juan J., Orra, Tarik H., and Ilario, Carlos. "SUAVE: An Open-Source Environment for Multi-Fidelity Conceptual Vehicle Design". *Proceedings of the 16th AIAA ISSMO Multidisciplinary Analysis and Optimization Conference* pp. 1–9. (22-26 2015). DOI: 10.2514/6.2015-3087.
[17] Torenbeek, Egbert. *Synthesis of Subsonic Airplane Design.* Kluwer Academic Publishers. Dordrecht, The Netherlands (1986). ISBN: 9024727243.
[18] Department of Defense, United States of America. "Military Specification: Flying Qualities of Piloted Airplanes." MIL-F-8785C. (1980).